Computers and Geotechnics 144 (2022) 104629

Contents lists available at ScienceDirect

Computers and Geotechnics

journal homepage: www.elsevier.com/locate/compgeo

Coupling of material point and continuum discontinuum element methods for simulating blast-induced fractures in rock

Zhongwen Yue [a], Jun Zhou [a], Chun Feng [b,*], Xu Wang [a], Linzhi Peng [a], Junyu Cong [c]

[a] School of Mechanics & Civil Engineering, China University of Mining and Technology (Beijing), Beijing 100083, China
[b] Key Laboratory for Mechanics in Fluid Solid Coupling Systems, Institute of Mechanics, Chinese Academy of Sciences, Beijing 100190, China
[c] Gdem Technology Co., Ltd, Beijing 100096, China

ARTICLE INFO

Keywords:
Continuum–discontinuum element method
Material point method
Rock blasting
Numerical simulation

ABSTRACT

A rock blasting simulation method is proposed that couples the material point method (MPM) and continuum discontinuum element method (CDEM). Blast-induced rock fractures are captured by the CDEM using normal and shear springs, and the explosive detonation is simulated by the MPM with a Jones-Wilkins-Lee equation of state. A particle–surface/edge contact method is introduced into the MPM-CDEM to calculate the interaction between the detonation products and rock medium. Three numerical examples are presented to verify the effectiveness of the proposed method. The fracture degree is represented as the ratio of the number of fractured springs to the total number of springs, and is used to analyze the evolution of shear and tension cracks under blasting. The simulation results show that the proposed numerical method well simulates blast-induced rock fractures and considers both progressive rock fracturing and the real explosive detonation. In particular, the expansion of the detonation gas, crushed zone around the blasthole, radial cracks, and effects of pre-existing stress on the blast-induced fractures are all successfully simulated.

1. Introduction

Blasting is a popular excavating method for breaking rock in underground space and is presently a hot topic in rock dynamics. The detonation of explosives involves a rapid chemical reaction and generates detonation products. However, the rock blasting fracture process is difficult to test owing to complex chemical reactions and multi-material interactions, as well as the expensive and time-consuming nature of laboratory and field experiments. Numerical methods therefore offer a promising alternative for investigating rock blasting fracture processes. The rapid advancement of computer technology in recent decades has also significantly improved the computation speed and accuracy for simulating various complex processes.

Several factors must be considered to accurately simulate complex rock blasting (e.g. geologic geometry, boundary conditions, material model) (Ainalis et al., 2016). Owing to the strong loading stress subjected to the rock mass, the simulations must account for high strain, high strain rates, and high nonlinear pressure distributions (Xie et al., 2019). Solid models, gas models, and solid–fluid interaction models are therefore the key components to establish a successful blast model (Zhu et al., 2008). Computational models for rock materials typically contain parameters related to the strength, failure, and equation of state (Huang et al., 2020). Considerable efforts have been made to simulate rock blasting in recent decades (Chen and Zhao, 1998; Donzé et al., 1997; Grady and Kipp, 1980; Hao et al., 2002a, 2002b; Ma et al., 1998; Toraño et al., 2006; Yang et al., 1996; Zhu et al., 2007). For example, Banadaki and Mohanty (Banadaki and Mohanty, 2012) used a Johnson-Holmquist model in the ANSYS AUTODYN software package to simulate single-hole rock blasting and investigate three distinct cracked regions around a borehole produced by shock/stress waves. Gao et al. (2018) showed that the influence mechanism of initiation location significantly affects the energy distribution, peak particle velocity, and rock damage during blasting. Wang et al. (2007) implemented the Taylor-Chen-Kuszmaul continuum damage model in the LS-DYNA software package to study the tension fracture behavior during blasting, as well as a blast crater near a free surface and the effects of charge modes on the blast crater. Peng et al. (2020) used LS-DYNA to simulate radial and circular cracks on the specimen surface and within its interior, and showed that crack propagation and crater shape are influenced by confining pressure. Pramanik and Deb (2015) implemented the smoothed particle hydrodynamics (SPH) framework to investigate the key physical phenomena of explosive detonation, expansion and failure of surrounding rock, and

* Corresponding author.
E-mail address: 644157990@qq.com (C. Feng).

https://doi.org/10.1016/j.compgeo.2021.104629
Received 16 April 2021; Received in revised form 30 December 2021; Accepted 30 December 2021
Available online 18 January 2022

the penetration of gaseous products during blasting. Their study revealed that the high crack density around the blast hole is caused by compressive stress, radial cracks are caused by the major principal stress, and spalling zones are caused by the reflected stress wave. Yan et al. (2016) considered both stress wave pressure and detonation gas pressure using a three-dimensional distinct element code method. Ning et al. (2011a) developed a discontinuous deformation analysis method to model bench blasting, identify the effect of explosion gas pressure on blast-induced fracturing, and analyze the pressure time history and rock fracture process. Xu et al. (2015) used the material point method (MPM) to model cylindrical charge blasting and identified three critical cracking zones in the vicinity of a tunnel.

Previous numerical methods used in blasting simulations can be summarized into two categories: continuum and discontinuum. Continuum numerical methods are appropriate for accurately describing rock deformation, but usually require a re-meshing technique for discontinuous problems, which leads to complicated and time-consuming blasting simulations. Although an erosion algorithm and the removal of damaged elements have been used to achieve an approximate solution for blast-induced fractures, the discarded eroded element volumes introduce inaccuracies into the algorithm (Gharehdash et al., 2020). Discontinuous numerical methods are therefore preferable for modeling discontinuous components in rock mass (e.g., faults, joints, bedding planes). In the discontinuum method, the rock mass is represented by an assembly of discrete elements/particles connected by contact units (e.g., springs, joints). The large element deformation and torsion problems in blasting simulations that cannot be solved using the continuous method are thoroughly improved when applying the discontinuous method. However, this approach requires a large amount of input data prior to calculation, which is frequently unavailable (Ma and An, 2008). A coupled method has therefore been attempted to simulate the rock failure evolution from continuum to discontinuum. An et al. (2017) used a hybrid finite-discrete element method (FEM-DEM) to simulate rock fracturing during blasting that was calibrated by comparing crushed, cracked, and long radial crack zones with values from literature. Han et al. (2020) used a combined FEM-DEM to model bench blasting in a deep tunnel. They pointed out that in-situ stresses have a strong effect on the stress redistribution pattern and failure evolution around tunnels. Jayasinghe et al. (2019) developed a coupled SPH and FEM model to understand the damage zone and fracture pattern in rock blasting and showed that discontinuity persistence and high in-situ stresses significantly influence the blast-induced damage and fractures. Fakhimi and Lanari (2014) proposed a hybrid numerical model for simulating rock failure and gas flow in rock blasting. Gas-rock interactions can generate successive compressive stress waves, which interact with and thus further extend radial cracks.

The aforementioned studies showed that the coupled method offers a considerably improved modeling technique in rock fracturing under blast loading that avoids the inherent single-method limitations. However, rock blasting simulations that consider the transition from continuous rock deformation to discontinuous fracturing and real explosive detonation processes have been scarcely reported (Fakhimi and Lanari, 2014; Pramanik and Deb, 2015). In this work, a coupled MPM and continuum discontinuum element method (CDEM) is proposed to simulate blast-induced rock fracturing. Previous studies have shown that the MPM can accurately simulate multi-physical phenomena involved in blasting and does not require time-consuming neighbor searching as in most meshfree methods (Hu and Zhen, 2006; Ma et al., 2009). CDEM combines the advantages of continuous and discontinuous techniques and can simulate progressive rock damage and failure evolution during blasting from a continuous field to a discontinuous field (Ding et al., 2021). In our coupled numerical method, the solid dynamic deformation and fracturing of rock mass and fluid flow of the detonation product are modeled using the CDEM and MPM, respectively. The solid–fluid interaction is achieved using a block–particle contact model. Some numerical examples of rock blasting are presented to demonstrate that the proposed numerical method is capable of simulating blast-induced fracturing.

2. Numerical methods

2.1. Material point method

The material point method (MPM) proposed by Sulsky et al. (1994) is a meshfree method. For hypervelocity impact problems, the MPM avoids the difficulty of mesh distortion commonly encountered in traditional mesh-based methods. The MPM also has the advantages of lower computational cost and higher accuracy. The computational domain in the MPM is represented by a finite number of discretized particles that can carry material variables (e.g. mass, stress, strain). However, the momentum equations are still calculated using a predefined background grid. The variable solution of these particles is divided into two steps: (1) particles are first rigidly deformed with the predefined background grid; and (2) the kinematic solution at the grid nodes is then mapped back to the particles to update their positions and velocities (Ma et al., 2009).

The governing formulation of the MPM is based on the weak form of the momentum equations and traction boundary condition (Zhang et al., 2010):

$$\delta\Pi = \int_V \rho\ddot{u}_i\delta u_i dV + \int_V \rho\sigma^s_{ij}\delta u_{i,j}dV - \int_V \rho f_i\delta u_i dV - \int_{\Gamma_t} t_i\delta u_i d\Gamma = 0 \tag{1}$$

where δu_i, ρ, $\ddot{u}$, σ_{ij}, f_i and t_i are the virtual displacement, density, acceleration, Cauchy stress, body force, and boundary traction, respectively, V denotes the material domain, and Γ denotes the material boundary.

The mass density of discretized particles can be given as:

$$\rho(x_i) = \sum_{p=1}^{n_p} M_p\delta(x_i - x_{pi}) \tag{2}$$

where M_p is the mass, n_p is the total number, δ is the Dirac delta function, and x_{pi} are the coordinates of particle p. Substituting the mass density into the weak form of the momentum equations yields:

$$\sum_{p=1}^{n_p} M_p\ddot{u}_{ip}\delta u_{ip} + \sum_{p=1}^{n_p} M_p\sigma^s_{ijp}\delta u_{ip,j} - \sum_{p=1}^{n_p} M_p f_{ip}\delta u_{ip} - \sum_{p=1}^{n_p} M_p t^s_{ip}h^{-1}\delta u_{ip} = 0 \tag{3}$$

where h^{-1} is the hypothetical thickness of the boundary layer to satisfy the volume integral requirement (Cheon and Kim, 2019).

In the MPM solution process, particles are rigidly attached to nodes of the background grid. At the end of each time step, particle velocities and positions are updated and a new regular grid is defined for the next time step. Hence, mesh distortion is avoid compared with the FEM. In MPM, the same computational grid is often used for all the time steps. Therefore, the same fixed regular grid can be used in all time steps. The mapping between particles and nodes can therefore be achieved by the finite element shape function of the nodes in the background grid:

$$u_{ip} = \sum_{g=1}^{8} N_{Ip}u_{iI} \tag{4}$$

$$u_{ip,j} = \sum_{g=1}^{8} N_{Ip,j}u_{iI} \tag{5}$$

where u_{ip}, u_{iI}, and $u_{ip,j}$ are the particle displacement, grid displacement, and derivative of the particle displacement, respectively; g is the total number of grid nodes of a finite element. For a hexahedron element, g = 8.

The MPM computational process of can be described as follows.

(1) Map the mass and momentum of the particles to the background grid to calculate the grid node variables:

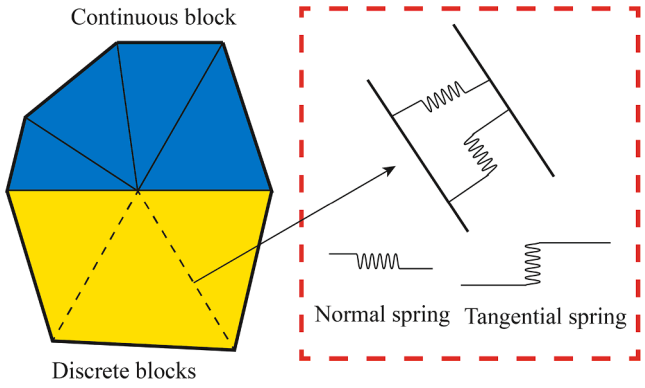

Fig. 1. Computational domain in the CDEM.

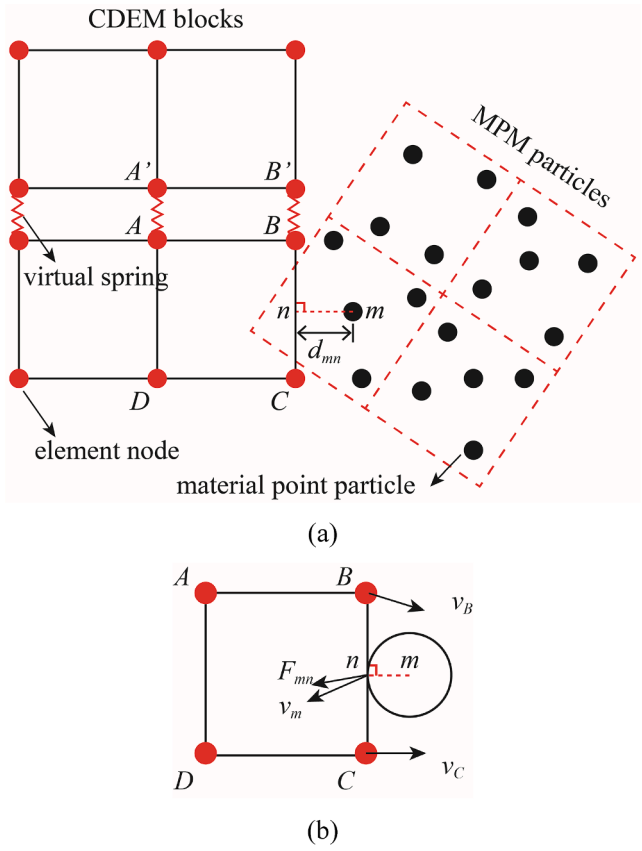

Fig. 2. Schematics of MPM–CDEM coupled analysis: (a) contact detection; (b) contact force calculation.

$$M_I^n = \sum_{p=1}^{n_p} M_p N_{Ip}^n \tag{6}$$

$$p_{iI}^{n-1/2} = \sum_{p=1}^{n_p} M_p v_{ip}^{n-1/2} N_{Ip}^n \tag{7}$$

where p and v denote the momentum and velocity, respectively, and the superscripts n and $n-1/2$ denote the time step.

(2) Impose boundary conditions on the momentum and update the velocity of grid nodes:

$$v_{iI}^{n-1/2} = p_{iI}^{n-1/2} / M_I^n \tag{8}$$

In this study, the material modeled by MPM did not have any particular boundary conditions. Therefore, boundary conditions for the displacement and normal stress were not used in the simulations.

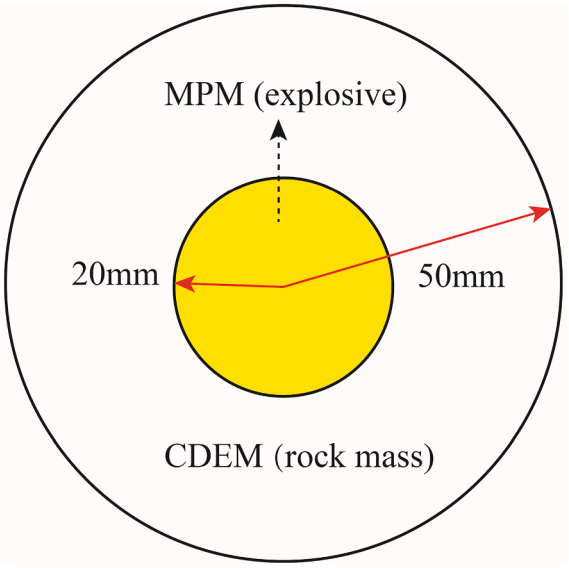

Fig. 3. Diagram of a circular rock medium containing a centrally located explosive.

Table 1
Parameters selected for emulsion explosive (An et al., 2018).

Material properties	Value
Density (kg/m^3)	1300
Detonation velocity (m/s)	4000
A (GPa)	214.4
B (GPa)	0.182
R_1	4.2
R_2	0.9
ω	0.15
E (GPa)	4.2

Table 2
Input parameters for the rock mass of the presented simulation.

Material properties	Value
Density (kg/m^3)	2600
Young's modulus (GPa)	50
Possion's ratio	0.2
Tensile strength (MPa)	10
Cohesion (MPa)	40
Internal friction angle (°)	40

(3) The incremental strain and density of the particles are calculated, and the incremental stress is accordingly updated by a constitutive model, as follows:

$$\Delta\varepsilon_{ijp}^{n-1/2} = \Delta t \sum_{I=1}^{8} \frac{1}{2}\left(N_{IP,j}^n v_{iI}^{n-1/2} + N_{IP,i}^n v_{jI}^{n-1/2}\right) \tag{9}$$

$$\rho^{n+1} = \rho^n / \left(1 + \Delta\varepsilon_{iip}^{n-1/2}\right) \tag{10}$$

(4) Calculate the force of the grid nodes:

$$f_{iI}^{int,n} = -\sum_{p=1}^{n_p} N_{Ip,j}^n \sigma_{ijp}^{n+1} \frac{m_p}{\rho_p^{n+1}} \tag{11}$$

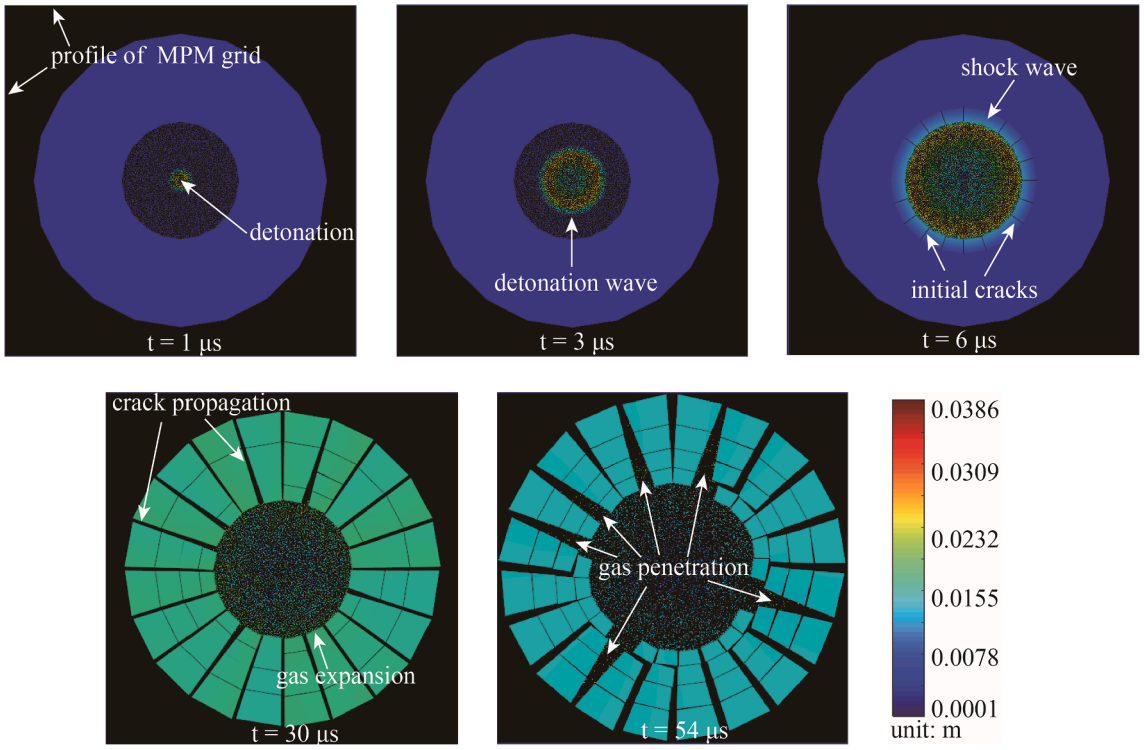

Fig. 4. Evolution of the displacement field of rock blasting at different time steps.

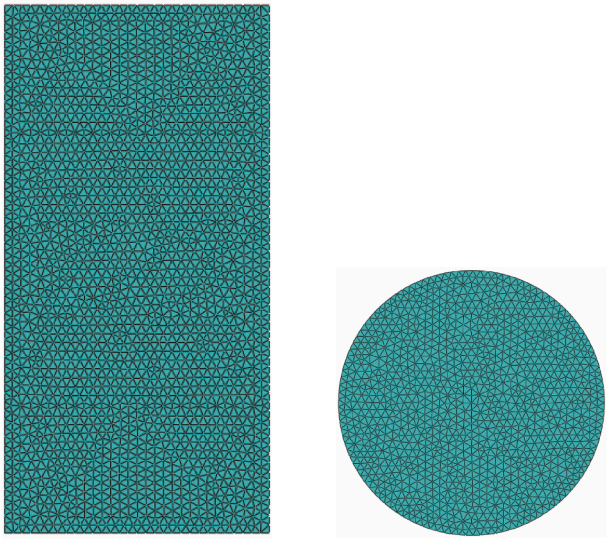

Fig. 5. Numerical models of: (a) uniaxial compressive test and (b) Brazilian disc test.

Table 3
Calibrated micro-properties in the CDEM.

Material properties	Value
k_n (GPa/m)	1,800,000
k_s (GPa/m)	1,600,000
Tensile strength (MPa)	14
Cohesion (MPa)	26
Internal friction angle (°)	60

Table 4
Calibrated results of rock properties in the CDEM.

Material properties	Calibrated	Target
Young's modulus (GPa)	50.8	51
Possion's ratio	0.18	0.16
Tensile strength (MPa)	7.4	7.3
Uniaxial compressive strength UCS (MPa)	162.3	161

$$f_{iI}^{ext,n} = \sum_{p=1}^{n_p} M_p N_{Ip}^n f_{ip}^n + \sum_{p=1}^{n_p} N_{Ip,j}^n t_{ip}^n h^{-1} \frac{m_p}{\rho_p} \tag{12}$$

$$f_{iI}^n = f_{iI}^{int,n} + f_{iI}^{ext,n} \tag{13}$$

where f_{iI}^n, $f_{iI}^{int,n}$, and $f_{iI}^{ext,n}$ are the total force, internal force, and external force, respectively.

(5) Integrate the momentum equation at the background grid note:

$$p_{iI}^{n+1/2} = p_{iI}^{n-1/2} + f_{iI}^n \Delta t^n \tag{14}$$

(6) Map the grid note variables to the corresponding particles to update the particle velocities and positions:

$$v_{ip}^{n+1/2} = v_{ip}^{n-1/2} + \Delta t^n \sum_{I=1}^{8} \frac{f_{iI}^n N_{Ip}^n}{m_I^n} \tag{15}$$

$$x_{ip}^{n+1} = x_{ip}^n + \Delta t^{n+1/2} \sum_{I=1}^{8} \frac{p_{iI}^{n+1/2} N_{Ip}^n}{m_I^n} \tag{16}$$

2.2. Continuum-discontinuum element method

As shown in Fig. 1, the computational domain of the CDEM generally contains intact blocks and discrete blocks that represent the FEM and DEM domains (Feng et al., 2014). In the CDEM, the DEM domain is divided into different discrete blocks from an original intact block. The

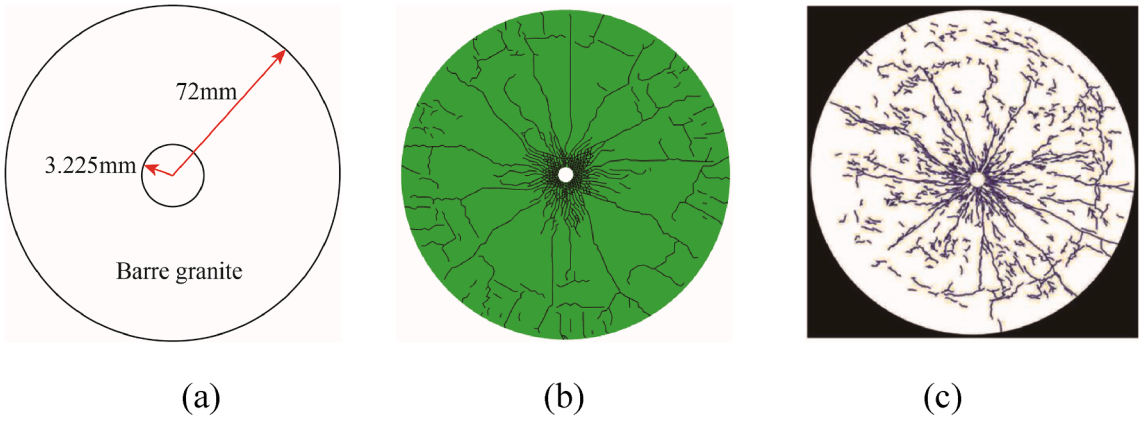

Fig. 6. Fracturing for a single-hole blast: (a) numerical model; (b) simulation by using presented example; (c) test of Banadaki 2010.

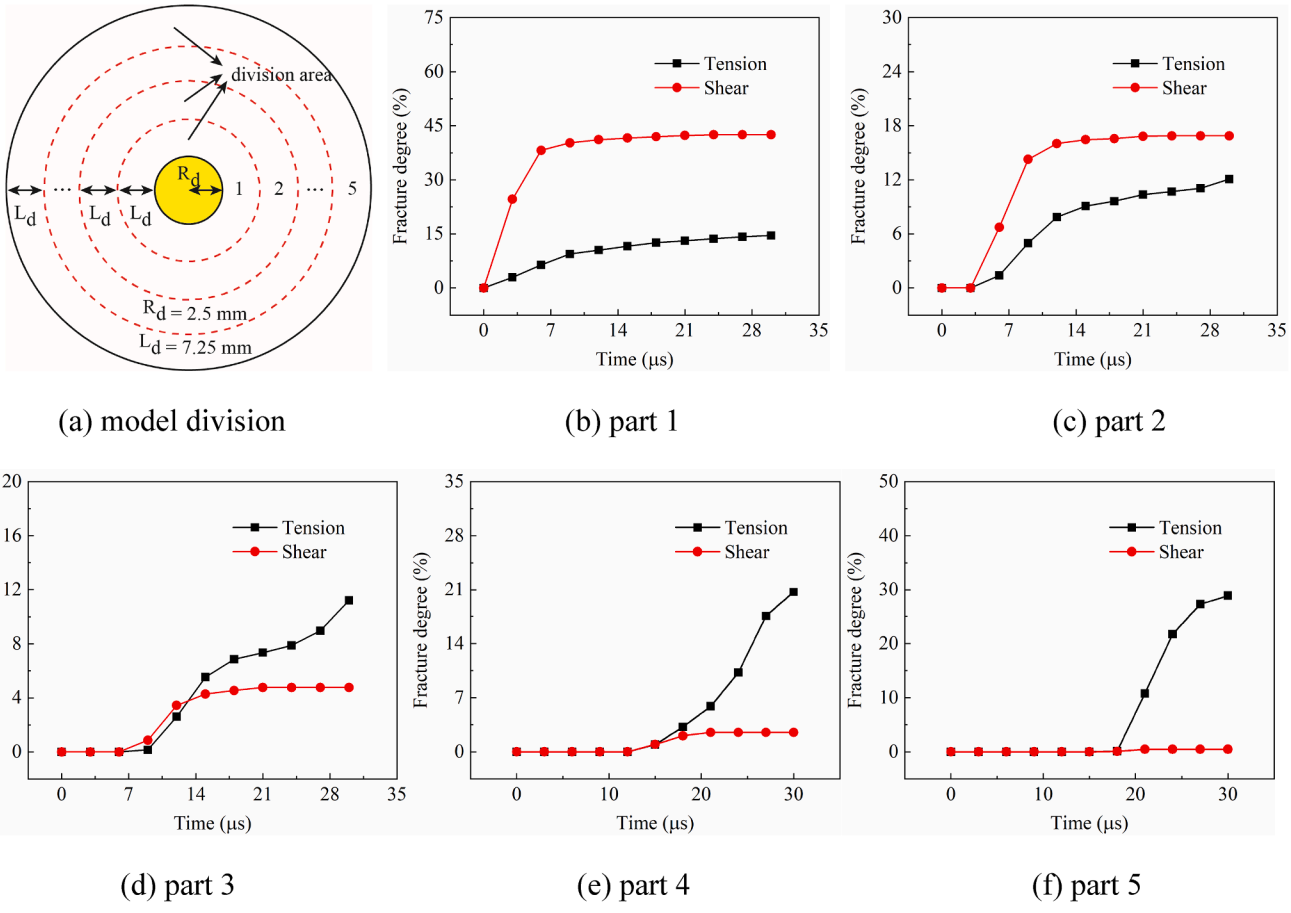

Fig. 7. Evolution of the fracture degree in each division.

interaction between these discrete blocks can be transformed into virtual spring forces. The forces at the contact interface of two blocks in the local coordinate can be expressed as:

$$F_{nt} = -K_{nt} \times \Delta u_{nt} \tag{17}$$

$$F_s = -K_s \times \Delta u_s \tag{18}$$

where F, K, and Δu are the incremental force, stiffness, and relative displacement of the virtual spring, respectively; nt and s represent the normal and tangential directions, respectively.

When a given failure criterion of the virtual springs is reached, the connected interface between the blocks is transformed into a discontinuous fracture surface. For a material in the CDEM, the tensile strength is governed by the maximum tensile stress criterion, and the shear strength is described by the Mohr-Coulomb model (Ma et al., 2016):

$$\text{Tensile strength model}: \quad \sigma_n \geqslant \sigma_f. \tag{19}$$

Shear strength model : $\tau \geqslant \sigma_n tan\alpha + C$.(20)where σ_n and τ are the spring forces in the normal and tangential directions, respectively, σ_f resprents the tensile strength, and C and α are the cohesion and internal friction angle, respectively.

In recent CDEM studies, the tensile fracture energy and shear fracture energy have also been used to respectively describe tensile and shear crack behavior (Zhang et al., 2020):

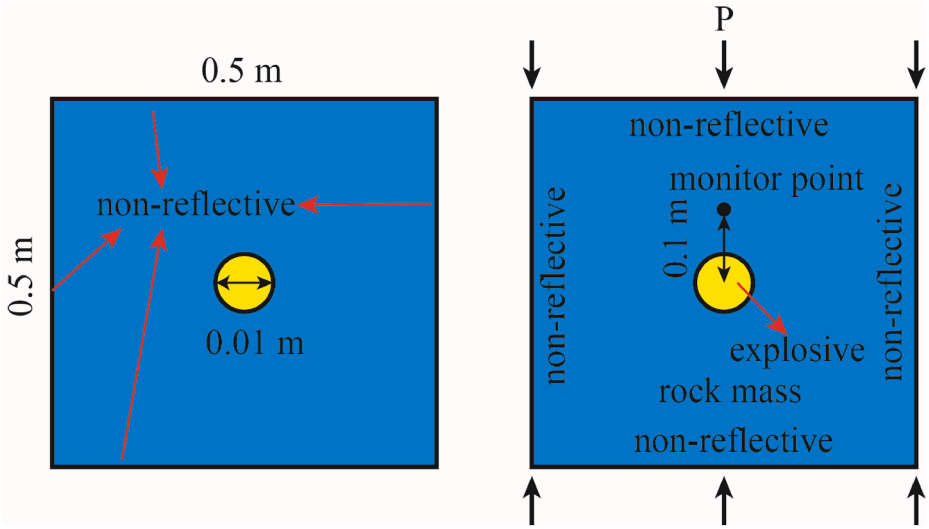

(a)

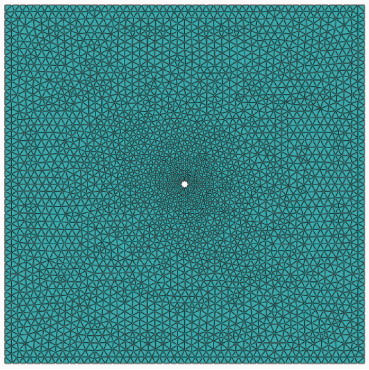

(b)

Fig. 8. Numerical modeling of a confined rock blast.

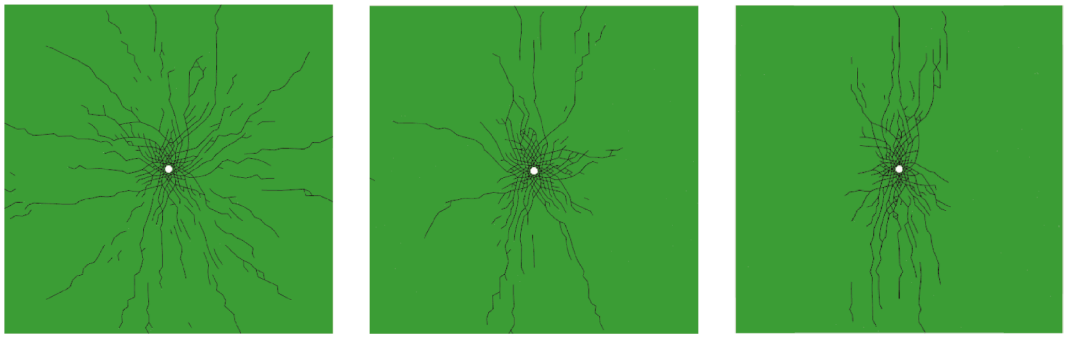

Fig. 9. Effect of pre-existing stress on blast-induced fractures.

$$\text{Tensile strength model}: \ \sigma_n(t_{i+1}) = -(\sigma_0)^2 \times \Delta u_n/(2G_{fn}) + \sigma_0 \tag{21}$$

$$\text{Shear strength model}: \ C_n(t_{i+1}) = -(C_0)^2 \times \Delta u_s/(2G_{fs}) + C_0 \tag{22}$$

where σ_0 and C_0 are the tensile strength and cohesion strength in the initial time step, respectively, Δu_n and Δu_s are the displacements in the normal and tangential directions, respectively, $G_{fn}$and G_{fs} are the tensile and shear fracture energy, respectively, and t_{i+1} denotes the next time step. Compared with Equations 19 and 20, the fracture energy is considered in the tensile strength and cohesion. However, the maximum tensile stress criterion and the Mohr–Coulomb model are still used in the fracture model. In this study, the fracture energy was not used to

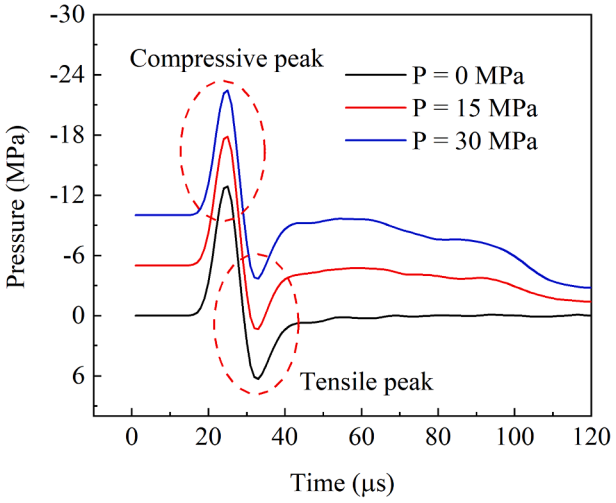

Fig. 10. Pressure-time curves at the monitor point under different confining conditions.

describe the tensile and shear crack behavior.

Dynamic problems can be efficiently modeled by considering the effect of dynamic inertia (Ju et al., 2018):

$$[M]\{u''\}+[C]\{u'\}+[K]\{u\}=\{F\}_{ext} \tag{23}$$

where $[M]$, $[C]$, and $[K]$ are the mass matrix, damping matrix, and stiffness matrix, respectively, and $\{F\}_{ext}$ is the external force vector:

$$\{F\}_{ext}=\{F\}_b+\{F\}_s+\{F\}_t \tag{24}$$

where $\{F\}_b$, $\{F\}_s$, and $\{F\}_t$ denote the body force, spring force, and boundary traction, respectively.

The CDEM calculation method is an explicit scheme and the nodal acceleration and nodal velocity of the elements can be calculated through the time-stepping scheme as follows:

$$\{a\}^n=\frac{\{u\}^{n+1}-2\{u\}^n+\{u\}^{n-1}}{(\Delta t)^2} \tag{25}$$

$$\{v\}^{n+1}=\frac{\{u\}^{n+1}-\{u\}^n}{\Delta t} \tag{26}$$

where n is the time step and Δt denotes the corresponding time step interval.

2.3. MPM–CDEM coupling

The MPM was selected to model the explosives for accurately simulating multi-physical phenomena involved in rock blasting. The rock material was modeled by the CDEM because of its accuracy and effectiveness of rock dynamic fracturing (Ding et al., 2021). Differing from the coupled FEM–MPM (Lian et al, 2011), the interaction between the CDEM domain and MPM domain is calculated by introducing a particle–surface/edge contact method (Xue et al., 2019). The contact model of the numerical simulation is illustrated in Fig. 2, and the contact is established by meeting the following requirements:

$$\begin{cases} d_{mn}\le R_m \\ d_{Bn}\le d_{BC} \\ d_{Cn}\le d_{BC} \end{cases} \tag{27}$$

where d and R denote distance and radius, respectively.

When the CDEM element is in contact with the material point particle, as shown in Fig. 2b, the normal and the shear contact force are calculated as follow:

$$\mathrm{F}_n(t+\Delta t)=\mathrm{F}_n(t)+k_n[(\mathrm{v}_m-\mathrm{v}_n)\Delta t]\cdot\mathrm{n}_n \tag{28}$$

$$\mathrm{F}_s(t+\Delta t)=\mathrm{F}_s(t)+k_s[(\mathrm{v}_m-\mathrm{v}_n)\Delta t]\cdot\mathrm{n}_s \tag{29}$$

where k represents the contact stiffness, and n represents the direction of the element edge. v_m is the velocity vector of the particle, and v_n is the velocity of the projection point of the particle m on the element edge:

$$\mathrm{v}_n=\frac{d_{Bn}}{d_{BC}}\mathrm{v}_B+\frac{d_{Cn}}{d_{BC}}\mathrm{v}_C \tag{30}$$

where v_B and v_C represent the velocity of the element nodes.

As mentioned above, a coupling scheme is proposed based on the particle–surface/edge contact method in the framework of MPM. In each time step, MPM bodies and CDEM bodies are first to detect whether they are in contact. If they are in contact, a contact force is applied to them to present the interaction. If they are not in touch, they are updated independently to the obtain information of nodal variables. To obtain stable solutions in numerical computations, the background cell should contain at least one material particle. Accordingly, the radius of particle does not exceed half the length of the background grid cell.

3. Numerical examples

The MPM has prominent advantages for solving large-deformation problems and efficiently simulates the explosive detonation process (Hu and Zhen, 2006; Ma et al., 2009). The efficacy of the CDEM for simulating brittle fractures in rock blasting has been verified in related literature (Ding et al., 2021; Yue et al., 2021). Therefore, the contact detection and contact force calculation are the key factor for the MPM-CDEM to ensure the accuracy of the numerical simulation. The accuracy of the block and particle coupling algorithm has also been verified for simulating blasting using the particle–surface/edge contact model (Xue et al., 2019). Several numerical examples are presented below to demonstrate the efficacy of the proposed coupling method in rock blasting.

3.1. Simulation of the rock blasting process

The objective of this example is to reveal the rock blasting process and understand the interaction between the explosive products and rock medium owing to the propagation of the detonation wave and expansion of high-pressure gas. A two-dimensional numerical model is established under plane strain conditions, as shown in Fig. 3. The cell size of the background mesh was set to 2 mm, and a background mesh with a size of 240 × 240 mm was used. Additionally, the particle radius was set to 0.2 mm, and a free boundary condition was set at the exterior of this model.

Two materials must be considered in this example, which are individually simulated by the MPM and CDEM. The detonation point is located at the center of the explosive and both the explosive and rock medium are within the range of the background grid. In the MPM domain, the Jones-Wilkins-Lee (JWL) equation is used to calculate the dynamic response of the explosive detonation. The JWL equation reflects the relationship between the expansion and pressure of the detonation products:

$$P=A\left(1-\frac{\omega}{R_1V}\right)\mathrm{EXP}(-R_1V)+B\left(1-\frac{\omega}{R_2V}\right)\mathrm{EXP}(-R_1V)+\frac{\omega E}{V} \tag{31}$$

where P represents the pressure of detonation products, A, B, R_1, R_2, and ω are material constants of the explosives, E denotes the detonation energy per unit volume, and V is the relative volume. An emulsion

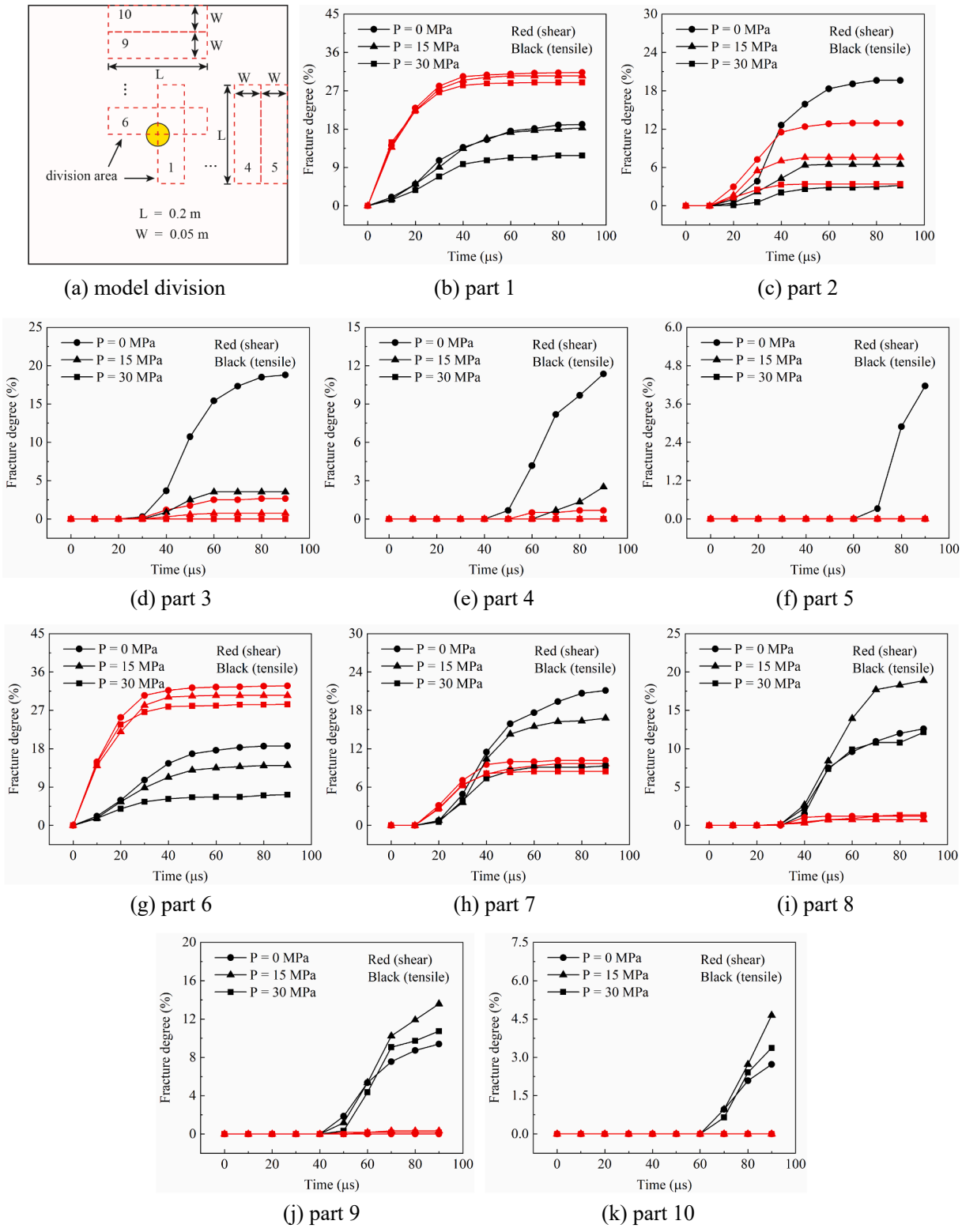

Fig. 11. Evolution of the fracture degree under different confining pressure conditions.

explosive is selected in the presented simulation, and its JWL equation of state parameters are listed in Table 1. In the CDEM domain, the rock properties are selected for the blasting simulations are listed in Table 2. For a block element, the incremental stress vector at Gauss point is calculated by incremental strain vector and the element's elasticity matrix. The failure of materials is judged by the contact state of the interface between different blocks. In this paper, the linear elastic fracture model expressed by Equations 19 and 20 is used for interface failure. Although the presented model does not directly consider strain-rate effects, the effects of loading rate on the rock strength can be achieved using a cohesive model and the discrete element method, which capture the interplay between inertial effects and fractures at the micro scale (Zhang et al., 2020).

Fig. 4 shows the rock blasting process from the explosive detonation

to rock fracturing. The initial cracks in the rock mass clearly form owing to the detonation wave on the borehole surface. The initial cracks propagate as the gas expands. Further growth of the radial cracks leads to crack opening near the borehole. The explosive gas then enters the interior of the fractured rock mass and acts on the surface of the opening cracks. The rock fracturing process is ultimately completed under the action of the high-pressure and explosive gas. In this case, 20 blast-induced radial cracks existed. Six blast-induced cracks further propagated at 54 μs, owing to the penetration of gas. Notably, the specific hole shape and mesh generation has a significant effect on the gas penetration.

3.2. Fracture pattern solution in a single-hole blast

A better understanding of the single-hole blast problem is the basis of rock blasting research. The typical single-hole blasting process usually involves borehole expansion, crushing close to the borehole, and fracturing outside of the crushing zone (Zhang, 2016). A single-hole blast model is simulated in this example. Unlike the previous case, the rock medium area is considerably larger than that of the explosive, which ensures that a complete fracture pattern can be formed in the rock mass.

In this simulation, the parameters were the same as those in the study of Banadaki and Mohanty (2012), who used pentaerythritol tetranitrate (PETN), a high explosive, in their model. The micro-mechanical parameters incorporated in the fracture models of CDEM are different from the macroscopic parameters measured in the laboratory. Therefore, a calibration procedure must be used to calibrate the micro-mechanical parameters including the normal and shear stiffness, tensile strength, cohesion, and frictional coefficient (Wu et al., 2018). CDEM micro-parameters are obtained by simulating uniaxial/triaxial compression and Brazilian tension tests. As shown in Fig. 5, all compressive samples measure 54 mm × 108 mm and a specimen of the Brazilian test has 54 mm diameter. The uniaxial compressive sample contains 3734 triangular elements and the Brazilian numerical model contains 2167 triangular elements. The calibration procedure is usually divided into three steps (Gao and Stead, 2014; Kazerani and Zhao, 2010; Saadat and Taheri, 2019): The first calibration step is to obtain the rock's Young's modulus and Poission's ratio. Using a trial-and-error procedure, the Young's modulus and Poission's ratio are obtained by altering the normal stiffness and shear-to-normal stiffness ratio. The second calibration step is to obtain the contact friction angle and cohesion. The last calibration step is to obtain the material tensile strength. The material tensile strength is only affected by contact tensile strength. Therefore, it can be calibrated by varying the contact tensile strength. The obtained input parameters are provided in Table 3 and calibration results are listed in Table 4.

Fig. 6 shows the fracture pattern of a single-hole blast. During the blast, when the high shock stress waves acted on the blasthole, a crushing zone first occurred in the vicinity of the blasthole. The shock waves are then attenuated to stress waves because of the energy consumed in the formation of the crushing zone. Several radial tension cracks form outside of the crushing zone owing to the stress wave action. Because the tensile strength of rock is substantially lower than its compressive strength, the proportion of tensile fractures in the fracture zone increases while the proportion of the compressive fractures strongly decreases. A free surface encountered during the propagation of stress waves will reflect stress waves. Tensile waves are then generated, and propagate into the rock from the free surface. Spalling then occurs around the free surface. The tensile waves propagate into the rock and interact with the preexisting cracks, and then the finally fracture pattern is formed. The results obtained by the simulations conducted using the MPM–CDEM revealed the fracturing of a single-hole blast. The above-mentioned results have also been reported by previous studies (An et al., 2017, 2018; Ning et al., 2011a, 2011b; Yan et al., 2016). However, in their studies, blasting effects are usually simplified as blasting waves which are applied to the boundary of blasthole in the numerical model.

The degree of fracturing in the rock blasting process is obtained to further investigate rock fracturing in single-hole blasting. The fracture degree is represented as the ratio of the number of fractured springs to the total number of springs (Zhang et al., 2020). The entire model is divided into equal parts (Fig. 7) and the fracture degree of each part is obtained. The explosive detonates at the beginning of the numerical calculation and the duration of detonation is 30 μs. The shear fracture degree markedly increases near the blasthole (part 1), whereas the variance of the tension fracture degree is slow. The shear fracture degree gradually decreases with increasing distance from the blasthole and ultimately becomes smaller than the tensile fracture degree. As shown in Fig. 7e and 7f, the tension fracture degree significantly increases, whereas the shear fracture degree remains close to zero. The above-mentioned results indicate that shear cracks formed close to the blasthole, owing to the high intensity of the shock waves inside the rock. Then, the energy was dissipated by the shock wave propagation. Owing to the relatively low tensile strength, shear fracture rarely occurred compared with tensile fracture. Additionally, owing to the existence of the free boundary, the propagating compression wave reflected onto a tensile wave to form a new tensile crack (An et al., 2017; Xie et al., 2017).

3.3. Effect of confining pressure on blast-induced fractures

Deep rock mass in engineering projects is subjected high in-situ stresses and the pre-existing stress has a significant effect on the blast-induced fractures.

Different models are established to simulate rock blasting under confining pressure ($P = 0$, 15, 30 MPa), as shown in Fig. 8. A plane strain numerical model is used in this example. The length and width of the rock geometry are 0.5 m and the blast hole diameter is 0.01 m. Triangular elements are used to discretize the numerical model of the rock mass. A fine mesh is used in the vicinity of the borehole where dense cracks may appear. Fig. 9 shows the rock blasting fracture pattern under different confining pressure conditions. The crushing zone occurs in the vicinity of the blasthole in all cases owing to the domination of the high shock waves. However, rock fracturing outside of the crushing zone is dominated by tensile stress. Fig. 9 shows that the propagation length of the radial cracks is considerably shorter in the horizontal direction than in the vertical direction. The simulation results indicate that high initial stress has a significant effect on rock fracturing during blasting (Yi et al., 2017). Fig. 10 shows the pressure–time curves at the monitor point under different confining stress conditions. The compressive peak increases with increasing confining stress, whereas the tensile peak decreases. This indicates that the confining stress can enhance the compression effect and weaken the tension effect of the blast-induced wave propagating along the radial direction of the borehole (Zhao et al., 2020).

Fig. 11 shows the evolution of the fracture degree under different confining pressure conditions. Ten divisions are created in the numerical model to calculate the fracture degree. Parts 1–5 are located continuously in the direction perpendicular to the confining pressure, whereas parts 6–10 are located continuously in the direction of confining pressure. Pre-existing stress is applied at the beginning of the numerical calculation and duration of detonation is 90 μs. In the horizontal direction, with increasing distance from the blasthole, the values of these curves are close gradually to zero except the tensile curve under the condition of $P = 0$, therefore these curves overlap. In the vertical direction, with increasing distance from the blasthole, only the shear curves overlap. The shear fracture degree gradually decreases with increasing distance from the blasthole. The tension fracture degree initially increases with increasing distance from the blasthole and then decreases. The pre-existing stress has a minor effect on the fracture degrees, as shown in Fig. 11b. However, the tension fracture degree and shear fracture degree both markedly decrease with increasing pre-existing stress outside of part 1, and the effect of pre-existing stress on

the fracture degrees gradually increases with increasing of the distance from the blasthole. A comparison of Fig. 11b and 11g shows that near the blasthole, the effect of pre-existing stresses on fracture degree in the direction perpendicular to the pre-existing stress is smaller than that in the confining pressure direction. However, this effect is larger in the direction perpendicular to the pre-existing stress with increasing distance from the blasthole than in the confining pressure direction, especially on the shear fracture degree (Fig. 11h–11k). As shown in Fig. 11i–11k, it is interesting to note that the final tension fracture degree is the largest under a pre-existing stress of 15 MPa and the smallest under the no-confining-pressure condition. This is because the vertical pre-existing stress limits crack growth in the horizontal direction. Cracks initiating and propagating from the blasthole are therefore deflected into the vertical direction. However, vertical crack growth gradually decreases with increasing pre-existing stress.

4. Discussion

The numerical simulations conducted using the proposed MPM-CDEM can capture the entire rock blasting process, from the explosive detonation, propagation of detonation waves, expansion of detonation products, and interaction of gas and rock to the eventual rock fracturing. Previous studies typically replaced the action of detonation products on the borehole using an assumed or theoretical gas-pressure time history (An et al., 2017; Han et al., 2020; Ning et al., 2011a, 2011b; Yan et al., 2016). As shown in Fig. 4, it is clear that in addition to gas expansion, the penetration of gas into opening cracks significantly affects crack propagation, which promotes further growth of the blast-induced cracks. The gas that penetrates into the opening cracks and action at the crack surface exhibits random behavior owing to the separation and rotation of the discretized block. Several opening cracks are therefore affected by the gas, which cannot be captured in rock blasting simulations using a gas-pressure time history.

Numerous attempts have been made to investigate blast-induced fracturing in rocks, the crushing zone near the blasthole, and radial cracks or spalling. However, there is not a single fracture mode in these specific fracture zones. In this study, the distribution of tensile and shear cracks is obtained in each specific fracture zone (Figs. 7, 11). The results indicate that the two crack modes evolve differently in the different fracture zones, which provides important insights on the fracture mechanism in rock blasting problems.

It is noted that the proposed model is limited in the simulations of rock blast-induced fracture behavior in terms of rock mass complexities (e.g., heterogeneities and natural defects). Further studies will therefore be useful to better understand crack initiation, propagation, and the interaction of blast-induced waves in rock blasting.

5. Conclusions

A coupled method is presented for efficiently simulating blast-induced fractures in rock. The MPM is used to simulate the explosive detonation process, which includes the propagation of high detonation pressure and movement of detonation products. The CDEM is used to reproduce the transition from continuum to discontinuum rock failure under blasting. The contact between material points of the MPM and blocks of the CDEM is detected using a particle–surface/edge contact method. Three numerical examples are presented to verify the effectiveness and accuracy of the proposed MPM in rock blasting. The main conclusions are summarized as follows.

(1) The entire process of rock blasting from explosive detonation, high pressure propagation and gas expansion, to rock fracturing can be reproduced using the coupled MPM-CDEM. The detonation products that penetrate into the opening cracks are also simulated.

(2) For single-hole rock blasting, the borehole expansion, crushing near the blasthole, and fracturing outside of the crushing zone are successfully simulated in the presented numerical model. The degree of shear fracturing markedly increases near the blasthole. The shear fracture degree substantially decreases with increasing distance from the blasthole, whereas the tension fracture degree gradually increases.

(3) Pre-existing stress has a significant effect on blast-induced cracks and can enhance the compression effect and weaken the tension effect of the blast-induced wave that propagates along the pre-existing stress direction. The effect of pre-existing stress on the fracture degree is smaller in the pre-existing stress direction than in the direction perpendicular to the pre-existing stress, especially in terms of the tension fracture degree. Cracks initiating and propagating from the blasthole are also deflected into the vertical direction owing to the effect of the vertical pre-existing stress. However, vertical crack growth gradually decreases with increasing pre-existing stress. The numerical examples indicate that the MPM-CDEM has great potential to simulate rock blast-induced fractures.

CRediT authorship contribution statement

Zhongwen Yue: Resources, Supervision, Project administration, Funding acquisition. **Jun Zhou:** Conceptualization, Investigation, Writing – original draft, Writing – review & editing. **Chun Feng:** Software, Methodology. **Xu Wang:** Formal analysis. **Linzhi Peng:** Formal analysis. **Junyu Cong:** Software.

Declaration of Competing Interest

The authors declare that they have no known competing financial interests or personal relationships that could have appeared to influence the work reported in this paper.

Acknowledgements

This research was supported by the National Natural Science of China (No.).

References

Ainalis, D., Kaufmann, O., Tshibangu, J.P., Verlinden, O., Kouroussis, G., 2016. Modelling the source of blasting for the numerical simulation of blast-induced ground vibrations: a review. Rock Mech. Rock Eng. 50 (1), 1–23. https://doi.org/10.1007/s00603-016-1101-2.

An, H.M., Liu, H.Y., Han, H., Zheng, X., Wang, X.G., 2017. Hybrid finite-discrete element modelling of dynamic fracture and resultant fragment casting and muck-piling by rock blast. Comput. Geotech. 81, 322–345. https://doi.org/10.1016/j.compgeo.2016.09.007.

An, L., Suorineni, F.T., Xu, S., Li, Y.H., Wang, Z.C., 2018. A feasibility study on confinement effect on blasting performance in narrow vein mining through numerical modelling. Int. J. Rock Mech. Min. Sci. 112, 84–94. https://doi.org/10.1016/j.ijrmms.2018.10.010.

Banadaki, M.M.D., 2010. Stress-Wave Induced Fracture in Rock Due to Explosive Action. University of Toronto.

Banadaki, M., Mohanty, B., 2012. Numerical simulation of stress wave induced fractures in rock. Int. J. Impact Eng. 40–41, 16–25. https://doi.org/10.1016/j.ijimpeng.2011.08.010.

Chen, S.G., Zhao, J., 1998. A study of UDEC modelling for blast wave propagation in jointed rock masses. Int. J. Rock Mech. Min. Sci. 35 (1), 93–99. https://doi.org/10.1016/S0148-9062(97)00322-7.

Cheon, Y.-J., Kim, H.-G., 2019. An adaptive material point method coupled with a phase-field fracture model for brittle materials. Int. J. Numer. Meth. Eng. 120 (8), 987–1010. https://doi.org/10.1002/nme.6167.

Ding, C., Yang, R., Feng, C., 2021. Stress wave superposition effect and crack initiation mechanism between two adjacent boreholes. Int. J. Rock Mech. Min. Sci. 138, 104622. https://doi.org/10.1016/j.ijrmms.2021.104622.

Donzé, F.V., Bouchez, J., Magnier, S.A., 1997. Modeling fractures in rock blasting. Int. J. Rock Mech. Min. Sci. 34 (8), 1153–1163. https://doi.org/10.1016/S1365-1609(97)80068-8.

Fakhimi, A., Lanari, M., 2014. DEM–SPH simulation of rock blasting. Comput. Geotech. 55, 158–164. https://doi.org/10.1016/j.compgeo.2013.08.008.

Feng, C., Li, S., Liu, X., Zhang, Y., 2014. A semi-spring and semi-edge combined contact model in CDEM and its application to analysis of Jiweishan landslide. J. Rock Mech. Geotech. Eng. 6 (1), 26–35. https://doi.org/10.1016/j.jrmge.2013.12.001.

Gao, F.Q., Stead, D., 2014. The application of a modified voronoi logic to brittle fracture modelling at the laboratory and field scale. Int. J. Rock Mech. Min. Sci. 68, 1–14. https://doi.org/10.1016/j.ijrmms.2014.02.003.

Gao, Q., Lu, W., Yan, P., Hu, H., Yang, Z., Chen, M., 2018. Effect of initiation location on distribution and utilization of explosion energy during rock blasting. Bull. Eng. Geol. Environ. 78 (5), 1–15. https://doi.org/10.1007/s10064-018-1296-4.

Gharehdash S., Barzegar M., Palymskiy I.B., Fomin P.A., 2020. Blast induced fracture modelling using smoothed particle hydrodynamics. International journal of impact engineering. 135, 103235.1-103235.22. doi: 10.1016/j.ijimpeng.2019.02.001.

Grady, D., Kipp, M.E., 1980. Continuum modelling of explosive fracture in oil shale. Int. J. Rock Mech. Min. Sci. Geomechanics Abstr. 17 (3), 147–157. https://doi.org/10.1016/0148-9062(80)91361-3.

Han, H., Fukuda, D., Liu, H., Fathi Salmi, E., Sellers, E., Liu, TingJin, Chan, A., 2020. FDEM simulation of rock damage evolution induced by contour blasting in the bench of tunnel at deep depth. Tunn. Undergr. Space Technol. 103, 103495. https://doi.org/10.1016/j.tust.2020.103495.

Hao, H., Wu, C., Seah, C., 2002a. Numerical analysis of blast-induced stress waves in a rock mass with anisotropic continuum damage models Part 2: Stochastic approach. Rock Mech. Rock Eng. 35 (2), 95–108. https://doi.org/10.1007/s006030200013.

Hao, H., Wu, C., Zhou, Y., 2002b. Numerical analysis of blast-induced stress waves in a rock mass with anisotropic continuum damage models Part 1. Equivalent Mater. Propert. Approach. 35 (2), 79–94. https://doi.org/10.1007/s006030200012.

Hu, W., Zhen, C., 2006. Model-based simulation of the synergistic effects of blast and fragmentation on a concrete wall using the MPM. Int. J. Impact Eng. 32 (12), 2066–2096. https://doi.org/10.1016/j.ijimpeng.2005.05.004.

Huang X., Kong X., Chen Z., Fang Q., 2020. A computational constitutive model for rock in hydrocode. International Journal of Impact Engineering. 145, 103687.1-103687.12. doi: 10.1016/j.ijimpeng. 2020.103687.

Jayasinghe, L.B., Shang, J., Zhao, Z., Goh, A.T.C., 2019. Numerical investigation into the blasting-induced damage characteristics of rocks considering the role of in-situ stresses and discontinuity persistence. Comput. Geotech. 116, 103207. https://doi.org/10.1016/j.compgeo.2019.103207.

Ju, Y., Wang, Y., Su, C., Zhang, D., Ren, Z., 2018. Numerical analysis of the dynamic evolution of mining-induced stresses and fractures in multilayered rock strata using continuum-based discrete element methods. Int. J. Rock Mech. Min. Sci. 113, 191–210. https://doi.org/10.1016/j.ijrmms. 2018.11.014.

Kazerani, T., Zhao, J., 2010. Micromechanical parameters in bonded particle method for modelling of brittle material failure. Int. J. Numer. Anal. Meth. Geomech. 34 (18), 1877–1895. https://doi.org/10.1002/nag.884.

Lian, Y.P., Zhang, X., Liu, Y., 2011. Coupling of finite element method with material point method by local multi-mesh contact method. Comput. Methods Appl. Mech. Eng. 200 (47–48), 3482–3494. https://doi.org/10.1016/j.cma.2011.07.014.

Ma, G.W., An, X.M., 2008. Numerical simulation of blasting-induced rock fractures. Int. J. Rock Mech. Min. Sci. 45 (6), 966–975. https://doi.org/10.1016/j.ijrmms.2007.12.002.

Ma, G.W., Hao, H., Zhou, Y.X., 1998. Modeling of wave propagation induced by underground explosion. Comput. Geotech. 22 (3–4), 283–303. https://doi.org/10.1016/S0266-352X(98) 00011-1.

Ma, K., Tang, C.A., Wang, L.X., Tang, D.H., Zhang, D.Y., Zhang, Q.B., Zhao, J., 2016. Stability analysis of underground oil storage caverns by an integrated numerical and microseismic monitoring approach. Tunn. Undergr. Space Technol. 54, 81–91. https://doi.org/10.1016/j.tust.2016.01.024.

Ma, S., Zhang, X., Qiu, X.M., 2009. Comparison study of MPM and SPH in modeling hypervelocity impact problems. Int. J. Impact Eng. 36 (2), 272–282. https://doi.org/10.1016/j.ijimpeng. 2008.07. 001.

Ning, Y., Yang, J., An, X., Ma, G., 2011a. Modelling rock fracturing and blast-induced rock mass failure via advanced discretisation within the discontinuous deformation analysis framework. Comput. Geotech. 38 (1), 40–49. https://doi.org/10.1016/j.compgeo.2010.09.003.

Ning, Y., Yang, J., Ma, G., Chen, P., 2011b. Modelling rock blasting considering explosion gas penetration using discontinuous deformation analysis. Rock Mech. Rock Eng. 44 (4), 483–490. https://doi.org/10.1007/s00603-010-0132-3.

Peng J., Zhang F., Du C., Yang X., 2020. Effects of confining pressure on crater blasting in rock-like materials under electric explosion load. International Journal of Impact Engineering. 139, 1035341.1-1035341.13. doi: 10.1016/j.ijimpeng.2020.103534.

Pramanik, R., Deb, D., 2015. Implementation of smoothed particle hydrodynamics for detonation of explosive with application to rock fragmentation. Rock Mech. Rock Eng. 48 (4), 1683–1698. https://doi.org/10.1007/s00603-014-0657-y.

Saadat, M., Taheri, A., 2019. Modelling micro-cracking behaviour of pre-cracked granite using grain-based distinct element model. Rock Mech Rock Eng. 52 (11), 4669–4692. https://doi.org/10.1007/s00603-019-01862-0.

Sulsky, D., Chen, Z., Schreyer, H.L., 1994. A particle method for history-dependent materials. Comput. Methods Appl. Mech. Eng. 118 (1–2), 179–196. https://doi.org/10.1016/0045-7825(94) 90112-0.

Toraño, J., Rodríguez, R., Diego, I., Rivas, J.M., Casal, M.D., 2006. FEM models including randomness and its application to the blasting vibrations prediction. Comput. Geotech. 33 (1), 15–28. https://doi.org/10.1016/j.compgeo.2006.01.003.

Wang, Z.L., Li, Y.C., Shen, R.F., 2007. Numerical simulation of tensile damage and blast crater in brittle rock due to underground explosion. Int. J. Rock Mech. Min. Sci. 44 (5), 730–738. https://doi.org/10.1016/j.ijrmms.2006.11.004.

Wu, W.D., Bai, J.B., Wang, X.Y., Yan, S., Wu, S.X., 2018. Numerical study of failure mechanisms and control techniques for a gob-side yield pillar in the sijiazhuang coal mine, china. Rock Mech. Rock Eng. 52 (6), 1231–1245. https://doi.org/10.1007/s00603-018-1654-3.

Xie, L.X., Lu, W.B., Zhang, Q.B., Jiang, Q.H., Chen, M., Zhao, J., 2017. Analysis of damage mechanisms and optimization of cut blasting design under high in-situ stresses. Tunn. Undergr. Space Technol. 66, 19–33.

Xie, L.X., Yang, S.Q., Gu, J.C., Zhang, Q.B., Lu, W.B., Jing, H.W., Wang, Z.L., 2019. JHR constitutive model for rock under dynamic loads. Comput. Geotech. 108, 161–172. https://doi.org/10.1016/j. compgeo.2018. 12.024.

Xu, L., Schreyer, H., Sulsky, D., 2015. Blast-induced rock fracture near a tunnel. Int. J. Numer. Anal. Meth. Geomech. 39 (1), 23–50. https://doi.org/10.1002/nag.2294.

Xue, K., Liu, J.Q., Feng, C., Gan, Y.X., Bai, C.H., 2019. Explosively driven hierarchical particle jetting. Chem Eng Sci. 202, 250–269. https://doi.org/10.1016/j.ces.2019.03.043.

Yan, P., Zhou, W., Lu, W., Ming, C., Zhou, C., 2016. Simulation of bench blasting considering fragmentation size distribution. Int. J. Impact Eng. 90, 132–145. https://doi.org/10.1016/j.ijimpeng. 2015.11.015.

Yang, R., Bawden, W.F., Katsabanis, P.D., 1996. A new constitutive model for blast damage. Int. J. Rock Mech. Min. Sci. Geomech. Abstr. 33 (3), 245–254. https://doi.org/10.1016/0148-9062(95)00064-X.

Yi, C., Johansson, D., Greberg, J., 2017. Effects of in-situ stresses on the fracturing of rock by blasting. Comput. Geotech. 104, 321–330. https://doi.org/10.1016/j.compgeo.2017.12.004.

Yue, Z., Zhou, J., Feng, C., Li, A., Qiu, P., Gang, M., 2021. Numerical investigation of the effect of holes on dynamic fracturing in multi-flawed granite. Fatigue Fract. Eng. Mater. Struct. 44 (7), 1883–1896. https://doi.org/10.1111/ffe.13474.

Zhang, X., Sze, K.Y., Ma, S., 2010. An explicit material point finite element method for hyper-velocity impact. Int. J. Numer. Meth. Eng. 66 (4), 689–706. https://doi.org/10.1002/nme.1579.

Zhang, Q., Zhi, Z., Feng, C., Cai, Y., Pang, G., Yue, J., 2020. Investigation of concrete pavement cracking under multi-head impact loading via the continuum-discontinuum element method. Int. J. Impact Eng. 135, 103410. https://doi.org/10.1016/j.ijimpeng.2019.103410.

Zhang Z.X., 2016. Rock fracture and blasting: theory and applications. Oxford, Elsevier Science. doi: 10.13140/RG.2.1.1498.2481.

Zhao, J.-J., Zhang, Y., Ranjith, P.G., 2020. Numerical modelling of blast-induced fractures in coal masses under high in-situ stresses. Eng. Fract. Mech. 225, 106749. https://doi.org/10.1016/j.engfracmech.2019.106749.

Zhu, Z.M., Mohanty, B., Xie, H.P., 2007. Numerical investigation of blasting-induced crack initiation and propagation in rocks. Int. J. Rock Mech. Min. Sci. 44 (3), 412–424. https://doi.org/10.1016/j.ijrmms.2006.09.002.

Zhu, Z.M., Xie, H.P., Mohanty, B., 2008. Numerical investigation of blasting-induced damage in cylindrical rocks. Int. J. Rock Mech. Min. Sci. 45 (2), 111–121. https://doi.org/10.1016/j.ijrmms.2007.04.012.